APL Photonics

RESEARCH ARTICLE | JANUARY 27 2025

On-chip power efficient MHz to GHz tunable Brillouin microwave photonic filters

Special Collection: Brillouin Scattering and Optomechanics

Reena Parihar ; Choon Kong Lai ; Ziqian Zhang ; Duk-Yong Choi ; Stephen J. Madden ; Benjamin J. Eggleton ; Amol Choudhary ; Moritz Merklein

APL Photonics 10, 010803 (2025)
https://doi.org/10.1063/5.0236905

AIP Publishing

APL Photonics ARTICLE pubs.aip.org/aip/app

On-chip power efficient MHz to GHz tunable Brillouin microwave photonic filters

Cite as: APL Photon. 10, 010803 (2025); doi: 10.1063/5.0236905
Submitted: 2 September 2024 • Accepted: 6 January 2025 •
Published Online: 27 January 2025

Reena Parihar,[1,a)] Choon Kong Lai,[2,3] Ziqian Zhang,[2,3] Duk-Yong Choi,[4] Stephen J. Madden,[4] Benjamin J. Eggleton,[2,3] Amol Choudhary,[1] and Moritz Merklein[2,3]

AFFILIATIONS

[1] Ultrafast Optical Communications and High-performance Integrated Photonics (UFO-CHIP) Group, Department of Electrical Engineering, Indian Institute of Technology (IIT), Delhi 110016, India
[2] The University of Sydney Nano Institute (Sydney Nano), School of Physics, The University of Sydney, Sydney NSW 2006, Australia
[3] Institute of Photonics and Optical Science (IPOS), School of Physics, The University of Sydney, Sydney NSW 2006, Australia
[4] Laser Physics Centre, Research School of Physics, The Australian National University, Australian Capital Territory, Canberra 2601, Australia

Note: This paper is part of the APL Photonics Special Topic on Brillouin Scattering and Optomechanics.
[a)] **Author to whom correspondence should be addressed:** Reena.Parihar@ee.iitd.ac.in

ABSTRACT

Stimulated Brillouin scattering (SBS) offers optically tunable, narrowband gain and loss resonances, which makes it ideal for optical filtering and signal processing applications. However, broadband filters utilizing Brillouin scattering typically necessitate multiple pump sources or linear frequency modulated waveforms, which necessitate the use of overall high pump powers to achieve broadband and multi-band filter configurations. To overcome the trade-off between bandwidth and power consumption, we introduce an on-chip broadband bandpass filter scheme leveraging the SBS response and the concept of radio frequency interference. We present the MHz to GHz reconfigurable microwave photonic filters on a chip. The bandwidth is tunable from 30 MHz to 1.2 GHz at a total pump power of only 15 dBm, corresponding to a figure of merit (maximum bandwidth/pump power) improvement of a factor of 25 compared to previously reported work. Furthermore, the filter exhibits frequency tuning capabilities ranging from 10 to 40 GHz (X to Ka-band) and can be configured from single- to multi-bandpass filter responses and switched from bandpass to bandstop.

I. INTRODUCTION

Radio frequency (RF) filters are essential for maintaining signal integrity in microwave and RF systems. They effectively eliminate unwanted signals, preserving the desired signals, which is key for various applications such as modern communication, signal processing, the Internet of Things (IoTs), radio astronomy, and radar.[1–5] Conventional RF filters using surface acoustic waves (SAWs) are compact but face limitations at higher frequencies and with bandwidth tunability. For example, SAW filters experience notable attenuation beyond 3.5 GHz.[6,7] In contrast, bulk acoustic wave filters can operate at X-band frequencies[8] but face fabrication challenges to extend their operation into millimeter-wave bands,[7,8] as well as bandwidth tunability limited to MHz. Yttrium iron garnet (YIG) filters offer extensive tuning capabilities, but their large size prohibits use in applications where size, weight, and power (SWaP) are critical.[9,10]

Microwave photonic (MWP) filters represent a new approach to tackling the challenges of bandwidth reconfigurability, frequency tuning, and SWaP performance in traditional RF filter systems. They harness the advantages of photonic components, which offer superior reconfigurability, broad tunability, and immunity to electromagnetic interference (EMI).[11,12]

Notably, most advanced MWP filters rely on large, costly fiber-optic components that are vulnerable to external distortions such as vibrations and temperature changes, making them unsuitable for small SWaP applications. To rival state-of-the-art RF filters, recent advancements in photonic integrated circuits (PICs), which encompass processing, modulation, and photodetection within compact footprints, have made it feasible to develop fully integrated MWP (IMWP) chips, meeting the stringent requirements of modern microwave systems.[13–15]

While IMWP filters have made significant strides in design and development, achieving high extinction ratios, challenges remain in improving resolution and thermal stability for RF sensing and communications.[16,17] For example, integrated optical microring resonators (MRRs) are commonly used to create compact on-chip MWP filters that can adjust both amplitude and phase responses.[18] However, these MRR-based MWP filters typically have a 3-dB bandwidth of around sub-GHz,[18] with a recent demonstration pushing toward 360 MHz[19] limited by waveguide losses.[18–20] They are also more sensitive to temperature variations and changes in input signal power caused by the thermo-optic coefficient,[21,22] and their operational range is constrained by their free-spectral range (FSR).

MWP filters implemented using optically tapped delay lines offer significant flexibility in tuning RF responses. However, their ability to resolve spectra is restricted to the GHz range because of the complex control required over the amplitude and phase of numerous optical filter taps,[23–25] and the passband-to-stopband extinction ratio is not very high. For example, these MWP filters employ optical comb generation, where each comb line undergoes further processing on a photonics chip, but their 3-dB bandwidth is constrained to MHz owing to the finite number of optical comb lines available.[26] Similar to MRR-based MWP filters, those utilizing optically tapped delay lines also face limitations in the operational frequency range due to their periodic response.

To achieve high-resolution signal processing, the well-known nonlinear optical effect stimulated Brillouin scattering (SBS) has garnered renewed interest for its potential use in IMWP filters due to their high spectral resolution following the initial demonstration of SBS in a photonic.[27] SBS relies on a third-order nonlinear acousto-optic interaction,[27–29] resulting in an exceptionally narrow optical resonant linewidth, typically around 10 MHz, limited by the acoustic phonon lifetime in the material. Unlike other methods, SBS does not suffer from FSR limitations, allowing for flexibility in the operational frequency range of the resulting MWP system. In addition, SBS in media such as optical fibers exhibits superior thermal stability in the Brillouin frequency shift compared to MRRs, as it is optically induced compared to relying on the structural resonance, offering advantages such as tunability and stability during MWP filter processing.[22,30]

To date, a maximum Brillouin gain of 52 dB has been achieved in As_2S_3 rib waveguides over centimeter scales.[31] Achieving bandwidth or multi-bandpass filters with SBS-based filters is difficult and necessitates specialized RF input waveforms, such as LFM waveforms,[32] or multiple gain pumps,[33] introducing complexity and reducing the power efficiency of systems, thereby limiting the tunability of the filter bandwidth.

In this work, we present an experimental investigation of a broadband tunable filter based on an As_2S_3 chalcogenide chip.[34] This filter achieves wide bandpass filtering capabilities by utilizing the SBS phase response generated from a single low-loss pump and gain pump coupled with RF interferometry. The filters demonstrated in our study exhibit reconfigurable bandwidth capabilities spanning over 5 octaves: 30 MHz to >1 GHz, with frequency agility ranging from 10 to 40 GHz, and can be switched from bandpass (BPF) and bandstop (BSF) filter responses. In comparison to previously reported filters,[33] our design improves bandwidth by a factor of ~3 and reduces power consumption by a factor of ~8. These advancements signify a significant improvement in the figure of merit (FOM), defined as the ratio of the bandwidth to the total SBS pump power by a factor of 25 times compared to the work previously reported.[33] This improvement leverages low-power Brillouin functionalities for next-generation communication systems and opens

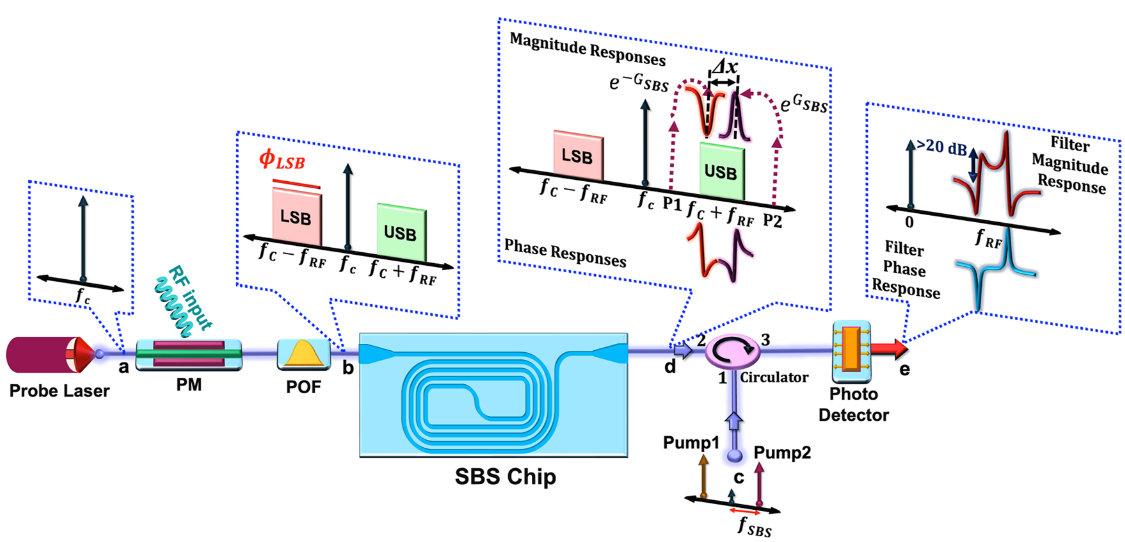

FIG. 1. Schematic of proposed on-chip broadband bandpass filter. (a) The output of the laser used as a probe signal, (b) the output of the programmable filter, (c) the pump signal input at the circulator's first port, (d) SBS Stokes and anti-Stokes response applied on the upper sideband after the pump–probe interaction, and (e) the output of the photodetector. PM: phase modulator; P1 and P2 are pump 1 and pump 2, respectively; and Δ*x*: separation between the peak SBS gain and loss applied on the USB.

up opportunities for integrating compact RF functionalities through hybrid photonic technologies.

II. PRINCIPLE OF OPERATION

The proposed broadband on-chip microwave photonic bandpass filter is achieved by cascading a phase modulator with a programmable optical filter to produce the probe signal. This probe signal subsequently interacts with the counter-propagating SBS Stokes and anti-Stokes pump signals.[35] The SBS gain and loss responses are applied on the upper sideband (USB) of the phase-modulated signal. Before the SBS interaction, the output of the phase-modulated signal is passed through a programmable optical filter (POF), which is the Finisar Waveshaper 1000A, to alter the amplitude and phase of the lower sideband (LSB) such that it forms a passband in between the region (marked by Δx) of Stokes and anti-Stokes response as shown in Fig. 1 (point d). Here, Δx represents the separation between the peak SBS gain and loss applied on the USB of the modulated link. The same effect can be realized by replacing the phase modulator and POF with a dual parallel Mach–Zehnder modulator (DPMZM) to vary the amplitude and phase of the lower sideband by precisely controlling the DC bias applied to DPMZM.

Figure 1 illustrates the principle of operation diagram of the proposed on-chip broadband filter utilizing stimulated Brillouin scattering. In this setup, the optical carrier frequency ω_c is generated using a probe laser, as shown in Fig. 1 (point a), which undergoes phase modulation by an RF signal at frequency ω_{RF}. This modulation generates two sidebands that are equal in amplitude but have a phase difference of π, which results in a DC signal after beating at the photodiode. However, by introducing a phase shift or amplitude offset to either or both sidebands, this cancellation condition can be disrupted, as shown in Fig. 1 (point *b*). At point c, pump 1 and pump 2 are generated using a pump laser source passed through an intensity modulator operated at double sideband suppressed carrier mode. At point *d*, the individual gain/loss and corresponding phase characteristics are applied to the upper sideband (USB) with a separation delta x (Δx). A negative phase region is observed between the Stokes and the anti-Stokes regions, based on the Kramers–Kronig relation. This introduces a phase difference between the two sidebands that is not equal to π while maintaining nearly equal amplitudes. The filter response can be observed at the output of the photodetector (e-point).

Furthermore, applying a positive phase deviation to the lower sideband of the phase-modulated link prevents cancellation in the central region because the phase difference between the sidebands is now less than π. Conversely, the phase difference in the regions to the left of the anti-Stokes region and to the right of the Stokes region remains nearly π, ensuring effective cancellation. The filter's magnitude and phase response obtained after photodetection are presented in Fig. 1 at point *e*.

The mathematical analysis of the filter response has been presented in the Appendix. The bandpass filter response is observed on a vector network analyzer (VNA) when the input RF frequency fed to the phase modulator is swept around ω_{RF}. The phase term ϕ_{USB} is completely controlled by the magnitude of the SBS gain and the loss pump and the spacing between both the pumps. ϕ_{LSB} is applied on the lower sideband of the phase-modulated signal and is completely controlled by the POF depending on the desired type of magnitude response at the VNA.

To analyze the filter passband and stopband response, Eq. (A10) in the Appendix (mathematical analysis) can be used. When the value of G_{USB} (the overall magnitude response due to the SBS gain and loss pump imparted on USB of the phase modulated link) approaches unity within the passband (marked by "Δx" in Fig. 1), at the same time, the corresponding SBS phase response ϕ_{USB} imparted within the passband of USB causes a negative phase shift, while the phase on the lower sideband ϕ_{LSB} is positive. This results in an offset in the amplitudes of the cosine waves, which violates the cancellation/destructive interference condition.

Similarly, at the stopbands on the blue shift of the SBS gain response and the redshift of the SBS loss response, G_{USB} remains close to unity. Although the phase of the cosine component ϕ_{USB} on the upper sideband is slightly positive. The negative cosine term exhibits a little positive phase, resulting in effective cancellation, hence creating a bandstop for all frequencies.

Due to an offset in the magnitude and phase response created by the individual SBS gain and loss response, the magnitude response near the passband edge is greater than that observed within the passband. It has been noted that the phase response of the filter is flat in the passband due to the SBS phase response ϕ_{USB} being flat in the passband of USB, as well as the phase response imparted on LSB ϕ_{LSB}, which is also constant.

Figure 2(a) shows the simulated results obtained for the reconfigurable bandpass filter by varying the pump frequency. The filter can be switched from bandpass to bandstop by altering the gain and

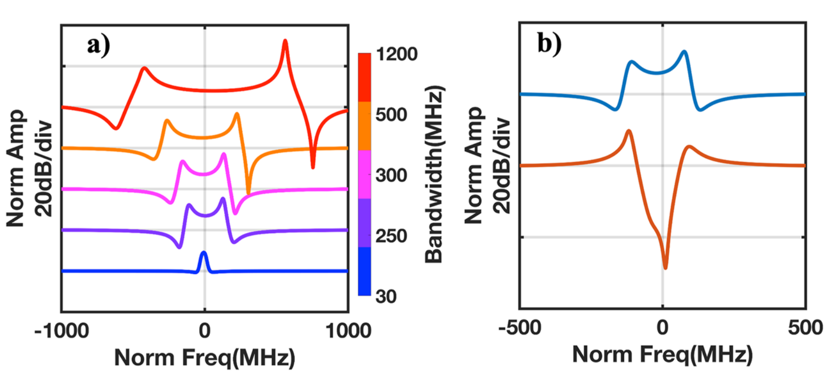

FIG. 2. Simulated (a) broadband reconfigurable BPF response by tuning the pump frequency and (b) switching from a bandpass to a bandstop response. Please note that each trace in 2(a) and 2(b) is translated by 20 dB.

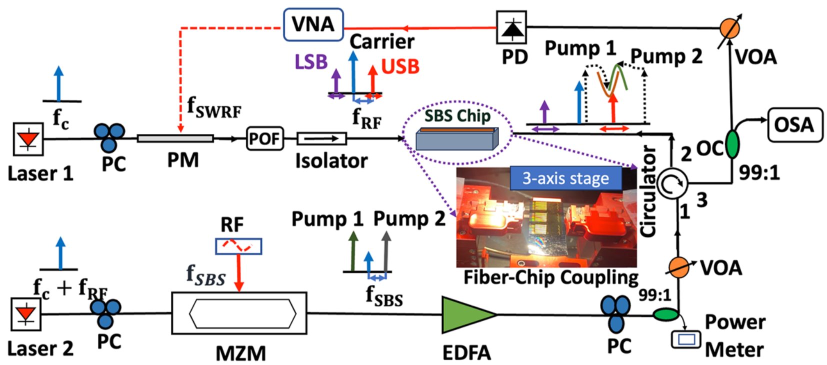

FIG. 3. Experimental setup of the low-power MWP filter. PC: polarization controller, VOA: variable optical attenuator, EDFA: erbium-doped fiber amplifier, OC: optical coupler, VNA: vector network analyzer, OSA: optical spectrum analyzer, PM: phase modulator, MZM: Mach–Zehnder modulator, POF: programmable optical filter, and f_{SWRF}: swept RF frequency. A photograph of the chip on the coupling stage is also shown.

loss response, as shown in Fig. 2(b). From the mathematical analysis, it has been observed that the phase response dominantly affects the filter response and, hence, can be used to vary the gain profile, which makes this approach power-efficient compared to tailoring the filter magnitude response by varying the pump power. It can be observed from the simulation that the filter exhibits significant magnitudes near the passband edges due to the phase and magnitude offset created by the individual SBS responses, resulting in higher magnitudes compared to those at the passband center.

III. EXPERIMENTAL SETUP AND RESULTS

The proposed on-chip broadband filter is achieved by using the SBS gain and the loss response applied on the phase-modulated link. Figure 3 shows the schematic of the experimental setup used to demonstrate the proposed filter. As shown in Fig. 3(a), laser 1 at frequency f_c has been phase-modulated by a swept RF signal with an instantaneous frequency of f_{SWRF}. When the f_{SWRF} is swept around the center frequency f_{RF}, this will generate two sidebands at frequency $f_c \pm f_{RF}$ that are equal in magnitude but are out of phase by π radian. Laser 2 at frequency $f_c + f_{RF}$ has been used to generate a pump after passing through the intensity modulator. An RF signal at frequency f_{SBS} has been used to modulate laser 2 to generate pump 1 and pump 2 at frequencies $f_c + f_{RF} \pm f_{SBS}$. An EDFA is used to amplify the pump power, which can be further controlled by a variable optical attenuator used after the EDFA.

The experiment is performed using a chip 11.7 cm in length with 15 turns (race track spiral) hybrid integrated As_2S_3–Ge:SiO_2 waveguide.[34] The design consists of a standard As_2S_3 rib waveguide (with a refractive index of 2.43, a width of 2.4 μm, a thickness of 0.96 μm, an etch depth of 33%, and supporting quasi-single mode operation) and a Ge:SiO_2 waveguide (with a core refractive index of 1.486, a square cross section of 3 × 3 μm^2, and supporting single mode operation), which extends to the end facets.[34] For fiber-to-chip coupling, an ultra-high numerical aperture (UHNA-3) fiber is utilized due to its low coupling and reflection losses. The coupling loss per waveguide facet is 0.85 dB, and the propagation loss is 0.5 dB/cm, resulting in a total loss of 10 dB. The achievement of low loss is facilitated by vertical tapering of As_2S_3 on germanosilicate glass.[34] The measured Brillouin shift and Brillouin gain coefficient g_B of the hybrid chip were found to be ≈7.8 GHz and 0.713 × 10^{-9} m W^{-1}, respectively. Figure 3 depicts the three-axis stage utilized for aligning the fiber with the chip during coupling.

The pump's interaction with the incoming probe signal in the waveguide induces SBS gain and loss on the USB of the phase-modulated signal. To create a bandpass filter, the separation between the Stokes and anti-Stokes signals is maintained at delta x (Δx). By applying the SBS Stokes and anti-Stokes responses, the phase and amplitude of the LSB are adjusted using a programmable optical filter at the output of the phase modulator. This achieves the desired bandpass characteristics based on the phase response within the passband at VNA in the region $\omega_c + \omega_{RF} - \frac{\Delta x}{2} < \omega < \omega_c + \omega_{RF} + \frac{\Delta x}{2}$, and bandstop in the $\omega > \omega_c + \omega_{RF} + \frac{\Delta x}{2}$ and $\omega < \omega_c + \omega_{RF} - \frac{\Delta x}{2}$ region after the photodetection. Subsection III A discusses the results obtained using the experimental setups described in Fig. 3.

A. Filter response

To achieve a filter response at 10 GHz, the frequency of laser 2 is set to laser 1 + 10 GHz. Given that the measured Brillouin shift for the As_2S_3 waveguide is 7.8 GHz, f_{SBS} is chosen as 7.8 GHz accordingly. The RF signal f_{SWRF} is swept across a range from 9.5 to 10.5 GHz to observe the complete filter response center at 10 GHz. Figure 4 illustrates the experimental and simulated magnitude response of

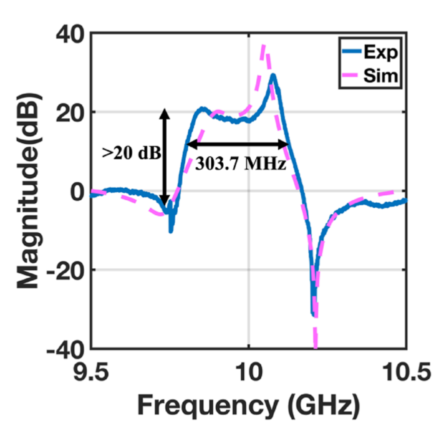

FIG. 4. Experimentally and simulated BPF response was obtained at a coupled pump power of 15 dBm. Sim: simulation and Exp: experimental.

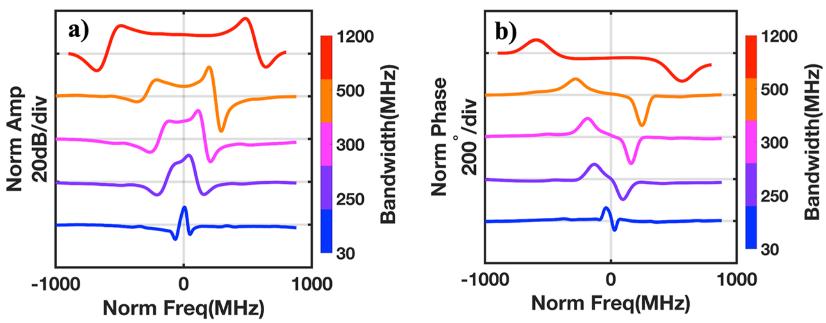

FIG. 5. Experimentally obtained bandwidth tuning of the bandpass filter response at a coupled pump power of 15 dBm. Please note that each trace is translated 20 dB more in panel (a) and 200° in panel (b).

the filter at a 10 GHz frequency, with a total pump power of 15 dBm. The measured passband-to-stopband ratio of the filter exceeds 20 dB.

The magnitude response of the bandpass filter in its passband is determined by the phase offset applied to the phase-modulated LSB signal using the POF. Variations in this phase offset cause changes in the filter's roll-off, impacting the level of suppression from passband to stopband. Therefore, selecting the optimal phase offset from POF is crucial to achieve effective suppression. It is observed that G_{USB} exhibits significant magnitudes near the passband edges due to individual SBS responses, resulting in higher magnitudes compared to those at the passband center.

B. Bandwidth tuning

The bandwidth reconfigurability of the MWP filter is achieved by controlling the frequency separation between the Stokes and anti-Stokes pump frequencies. The filter's bandwidth, defined as the 3-dB bandwidth relative to the center frequency of its passband, is measured from 30 MHz to 1.2 GHz at a total pump power of 15 dBm, significantly exceeding the individual SBS response of about 30 MHz. Figure 5(a) illustrates the magnitude response of the filter, while Fig. 5(b) shows its corresponding phase response. This result represents an improvement of ~3 times compared to the previously demonstrated bandwidth of 440 MHz,[33] achieved using approximately one-eighth of the pump power, which improved the FOM (the ratio of tunable bandwidth to power) by 25 times compared to work reported in Ref. 33.

C. Central frequency tuning

The bandpass filter responses are depicted at various central frequencies by adjusting the pump laser frequency, as depicted in Fig. 6(a). The filter demonstrates frequency versatility ranging from 10 to 40 GHz. The lower central frequency constraint of 10 GHz is due to the resolution capability of the POF, while the upper central frequency limitation of 40 GHz is determined by the frequency constraints of the VNA. Figure 6(b) shows the corresponding phase response at different central frequencies. As illustrated in Fig. 6(a), the filter response lacks symmetry due to the SBS phase response corresponding to the individual gain and loss pump, as shown in Fig. 1 (point d).

D. Switchable bandpass to bandstop response

The demonstrated filter can smoothly be tuned from a bandpass configuration, featuring a 3 dB bandwidth of 144 MHz, to a bandstop configuration with a 3 dB bandwidth of 280 MHz. This transition can be achieved either by adjusting the phase of the lower sideband using POF or by altering the gain and loss responses. Figure 7(a) displays the BPF response achieved through optimal phase adjustment of the LSB in the phase-modulated link using POF. Figure 7(b) illustrates the switch to a BSF response, while Figs. 7(c) and 7(d) depict the corresponding phase responses.

E. Multi-bandpass response

Figure 8 depicts the pump configuration utilized for generating the multi-filter response. The probe setup used to generate the

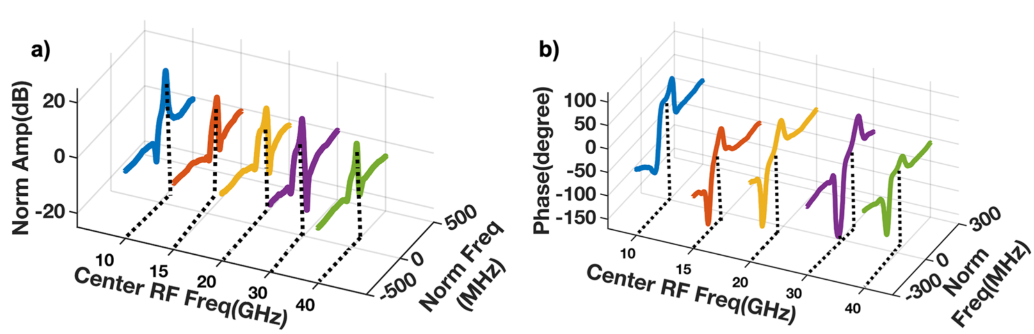

FIG. 6. Center RF frequency tuning of the on-chip filter at a pump power of 15 dBm. (a) Magnitude response and (b) the corresponding phase response.

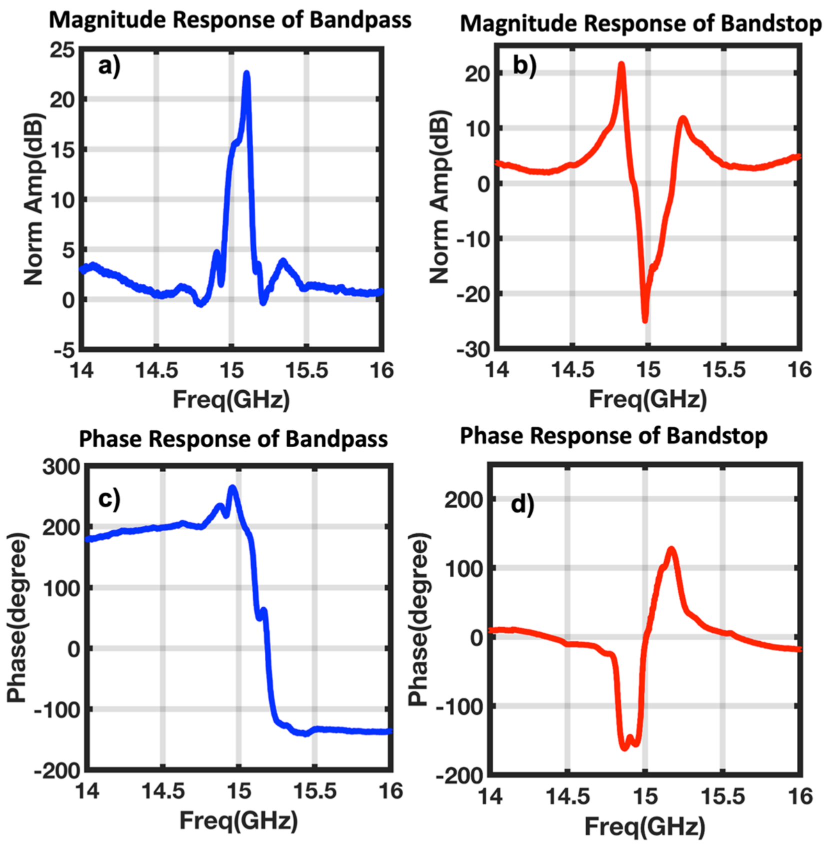

FIG. 7. Experimentally obtained switchable bandpass to bandstop filter response. (a) BPF magnitude response, (b) the BSF magnitude response, (c) the BPF phase response, and (d) the BSF phase response.

multi-filter response is the same as that used in Fig. 3. The primary distinction between the two setups lies in the pump configuration. Figure 3 shows the setup employing a single RF signal at the MZM to generate the pump, while Fig. 8 utilizes two RF signal generators (SG1 and SG2) to create a multi-pump setup. In addition, Fig. 8 substitutes the MZM with a DPMZM and adjusts the DC bias to generate a lower sideband alongside the carrier. These two lower sidebands, along with the optical carrier, serve as pumps spaced evenly by 2 * f_{SBS}, facilitating the transfer of gain and loss responses onto the upper sideband of the phase-modulated signals depicted in Fig. 8.

The lower sideband generated by the DPMZM serves as pumps P_{LSB1} and P_{LSB2}, while the optical carrier fed to the DPMZM acts as the pump P_{PC}. It is important to note that the frequencies of

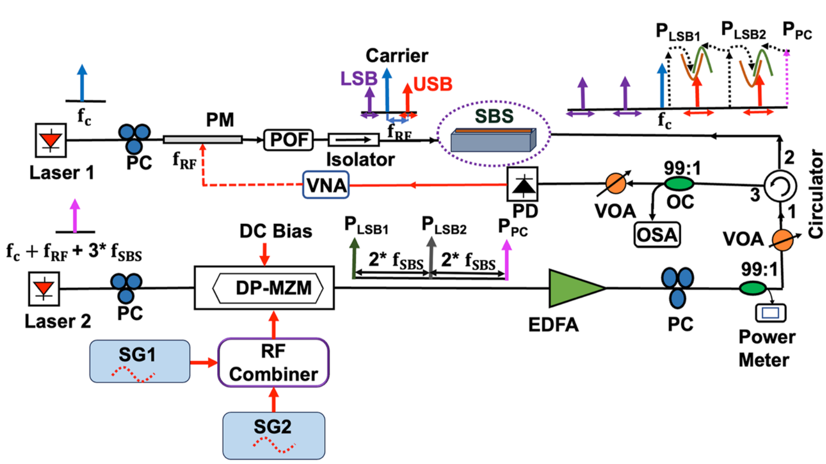

FIG. 8. Experiment setup used to generate the multi-bandpass response. SG: signal generator; and P1, 2, and 3: pump 1, 2, and 3.

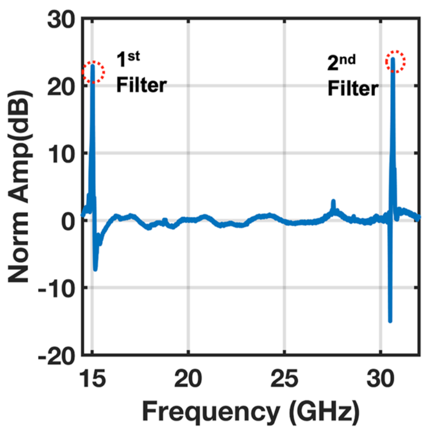

FIG. 9. Measured multi-bandpass response at a pump power of 13 dBm.

both signal generators are selected such that the spacing between the individual pumps P_{LSB1}, P_{LSB2}, and P_{PC} is maintained at 2 * f_{SBS}. This spacing of 2 * f_{SBS} ensures a symmetric bandpass response is observed at a distance of SBS from each individual pump after the pump–probe interaction, as illustrated in Fig. 8.

The VNA trace illustrates the bandpass filter responses at 15 and 30.6 GHz, depicted in Fig. 9. The first filter response is attributed to the transfer of anti-Stokes and Stokes responses by pumps P_{LSB1} and P_{LSB2}, respectively. Simultaneously, the second filter response arises from the transfer of anti-Stokes and Stokes responses by pumps P_{LSB2} and P_{PC}, respectively. The asymmetry in the filter response can be adjusted by altering the polarization. In addition, the filter response can be tuned by adjusting the frequencies of the signal generators (SG1 and SG2) while maintaining the pump spacing at 2 * f_{SBS}.

Figure 9 illustrates that the spacing between both bandpass filters is 2 * f_{SBS}, with f_{SBS} measured at 7.8 GHz for the As_2S_3 chip used in this study. The spacing between the filters can be varied by using signal generators with more than two outputs or by employing a programmable optical filter at the pump side to selectively control the pumps generated at the output of the DP-MZM, adjusting the DC bias differently from that used in this experiment.

IV. DISCUSSION

To evaluate the overall performance of the proposed microwave photonic filter, we compare it with state-of-the-art electronic and MWP filters, as shown in Table I. It has been observed that the filter design using MWP techniques performs better than the electronic one in terms of bandwidth tunability and central frequency tuning range. Following the progress and breakthroughs in fiber-based devices, tremendous effort has been made in past decades to harness SBS in compact, low-power, chip-scale MWP platforms.

On-chip integrated silicon nanowires on oxide have the issue of inherent acoustic guidance, which mandates under-etched and suspended complex structures and suffers severe nonlinear optical losses that limit Brillouin's gain at the optical telecommunication wavelength. On the other hand, an SBS chip made from silicon nitride (Si_3N_4)[43,44] has almost no nonlinear loss, but its SBS gain

TABLE I. State-of-the-art electronic and MWP bandpass filter's performance comparison.

Technology		Bandwidth (Min)	Bandwidth (Max)	Central frequency tuning range	Filter switchability	Multiple filter	Optical power used	FOM	References
Electronic	SAW filter	⋯	213 MHz	Only 1.28 GHz	⋯	⋯	⋯	⋯	36
	BAW filter	190 MHz	380 MHz	<8 GHz	⋯	⋯	⋯	⋯	7
	YIG filter	50 MHz	87 MHz	11–16 GHz	⋯	Yes	⋯	⋯	37
MWP (without SBS)	Optical filter tap	⋯	3.5 GHz	Upto 43.9 GHz	⋯	Yes	⋯	⋯	38
	Optical MRR	380 MHz	450 MHz	3–25 GHz	BPF to BSF	Yes	⋯	⋯	19
	SOI	1.93 GHz	⋯	3–10 GHz	⋯	⋯	⋯	⋯	39
	SOI	170 MHz	⋯	2–18.4 GHz	⋯	Yes	11.58 dBm	⋯	40
	InP + SOI	360 MHz	470 MHz	3–21 GHz	BSF to BPF	⋯	⋯	⋯	19
MWP (with SBS)	MRR	0.5 GHz	4.6 GHz	2–6 GHz,2–14 GHz	⋯	Yes	30.5 dBm	⋯	41
	SMF	30 MHz	705 MHz	8.14–22.3 GHz	⋯	⋯	14 dBm	28	4
	SOI	5.3 MHz	⋯	4–10 GHz	⋯	Yes	⋯	⋯	42
	Si_3N_4	4.54 GHz	9.72 GHz	4–25 GHz	BSF to BPF	Yes	⋯	⋯	43
	As_2S_3	30 MHz	440 MHz	3–30 GHz	BPF to BSF	Yes	24.47 dBm	1.5	33
	This work	30 MHz	1.2 GHz	10–40 GHz	BPF to BSF	Yes	15dBm	38	

coefficients are smaller because of its inherent material properties of a very low elasto-optic coefficient. In contrast, photonic chips using soft chalcogenide glasses (As_2S_3) feature a significantly higher elasto-optic coefficient and effectively confine both acoustic and optical modes. This characteristic results in markedly increased Brillouin gain coefficients, achieving substantial SBS gain (>30 dB) even within a smaller footprint area.[31,45,46]

As mentioned in Sec. I, a Brillouin gain of 52 dB has been achieved in As_2S_3 rib waveguides over centimeter scales.[31] Such results have strengthened the position of the high index contrast As_2S_3 platform as a strong contender to realize practical SBS-based MWP sources and filters, which are key components in integrated microwave photonic (IMWP) systems. In this work, an approach[34] to mitigate high coupling losses associated with optical fibers, which result from their small effective mode area and back reflections, has been employed. The use of high-index contrast germanosilicate, a mature platform, addresses issues related to back reflections and fiber coupling losses, thereby enhancing non-linearity and functional capabilities. This approach also facilitates the implementation of very narrow bandwidth filtering.

The approach used in this work for creating a chip-based RF broadband tunable filter is simpler and more power-efficient than the one detailed in Ref. 33. This method utilizes the phase response of stimulated Brillouin scattering combined with RF interferometry to achieve broad bandpass filtering with just one low-power gain and one loss pump. In contrast, the method in Ref. 33 required multiple pumps to achieve a similar broadband response. Our technique allows for bandwidth reconfiguration from 30 MHz to 1.2 GHz with a total pump power of 15 dBm, which corresponds to a FOM (maximum bandwidth/pump power) of 38 MHz/mW. Meanwhile, in Ref. 33, a total pump power of 24.47 dBm was used to achieve bandwidth reconfigurability from 30 to 440 MHz, which corresponds to a FOM of 1.5 MHz/mW. In comparison, the work presented in this paper[33] resulted in an overall improvement of FOM by 25 times. In addition, the central frequencies of the filter can be tuned from the X-band to the Ka-band by adjusting the pump frequencies, making it highly applicable for radar, satellite communications, military and defense, and aerospace industries.

However, chalcogenide waveguides are typically limited to realizing only the MWP filter system, while other essential components, such as electro-optic modulators (EOMs) and photodetectors (PDs), may need to be located off-chip. Although the compatible silicon-on-insulator (SOI) platform has successfully demonstrated heterogeneous integration of passive silicon waveguides with chalcogenide-based Brillouin circuits,[47] integrating E–O interfaces still presents challenges for SWaP-C^2 improvements. Therefore, achieving integrated feasibility among EOMs, chalcogenide-based Brillouin circuits, and PDs is crucial for enhancing the SWaP-C^2 profile of MWP chips.[29]

In this work, to adjust the suppression ratio or switch between bandpass and bandstop modes, the phase offset applied by the POF (Finisar Waveshaper 1000A) to the lower sideband must be varied. This adjustment process of POF takes 500 ms to stabilize. In addition, the POF used in this paper has a resolution capability of 8 GHz, which limits the minimum achievable filter's central frequency to 10 GHz. To achieve the ideal filter response, the phase offset applied on the lower sideband must be increased to get a steeper filter roll-off, although this comes at the cost of a reduced passband level.[4] At lower offsets, the passband level is higher, but the roll-off is less pronounced. An optimal phase shift can be selected based on the specific application to fine-tune the filter's response.

V. CONCLUSION

This paper introduces a chip-based RF tunable filter utilizing SBS phase response and RF interferometry for achieving broad tunability. This innovative approach enables broad bandpass filtering capabilities using a single low-power gain and loss pump. Our filter demonstrates adjustable bandwidth ranging from 30 MHz to over 1.2 GHz, covering more than five octaves with an FOM of 25 times better than showed prior.[33] It allows tuning of the central frequency from 10 to 40 GHz and supports switching between bandpass (BPF) and bandstop (BSF) responses with a passband to stopband selectivity exceeding 20 dB at a total pump power of 15 dBm. In comparison to previous studies,[33] our filter achieves more than a twofold increase in bandwidth and reduces power consumption by approximately eightfold. The low-power Brillouin filters demonstrated offer a pathway for implanting compact RF functionalities through hybrid photonic integration technologies.[47]

ACKNOWLEDGMENTS

We acknowledge the support from the Department of Telecommunications (DoT), India, through the Advanced Optical Communications Testbed Project. We also acknowledge the support of the Australian Research Council (Grant Nos. DP220101431 and DP200101893) and the Australian Research Council Center of Excellence in Optical Microcombs for Breakthrough Science (Project No. CE230100006). RP acknowledges the Prime Minister's Research Fellows (PMRF) Scheme.

AUTHOR DECLARATIONS

Conflict of Interest

The authors have no conflicts to disclose.

Author Contributions

Reena Parihar: Methodology (lead); Visualization (lead); Writing – original draft (lead); Writing – review & editing (lead). **Choon Kong Lai**: Methodology (equal); Writing – review & editing (equal). **Ziqian Zhang**: Methodology (equal); Writing – review & editing (equal). **Duk-Yong Choi**: Methodology (equal); Writing – review & editing (equal). **Stephen J. Madden**: Methodology (equal); Writing – review & editing (equal). **Benjamin J. Eggleton**: Funding acquisition (equal); Project administration (equal); Writing – review & editing (equal). **Amol Choudhary**: Conceptualization (lead); Funding acquisition (equal); Supervision (equal); Writing – review & editing (equal). **Moritz Merklein**: Investigation (equal); Methodology (equal); Supervision (equal); Writing – review & editing (equal).

DATA AVAILABILITY

The data that support the findings of this study are available from the corresponding author upon reasonable request.

APPENDIX: MATHEMATICAL ANALYSIS

The mathematical analysis of the SBS gain and loss response and the corresponding phase response of the phase-modulated link has been derived. The complex SBS gain $G_{SBS}(\omega)$ is given by[3]

$$G_{SBS}(\omega) = \frac{g_B P_p L_{eff}}{A_{eff}} \frac{1}{1 - 2j(\Delta\omega/\Gamma_B)}, \quad (A1)$$

where A_{eff} is the effective mode area, L_{eff} is the effective length of the waveguide, g_B is the Brillouin gain coefficient, Γ_B is the Brillouin linewidth, P_p is the pump power, and $\Delta\omega$ is the frequency-detuning in rad/s from peak SBS gain. Here, $\Delta\omega = \omega - \omega_0$ and ω_0 is the frequency where peak SBS gain occurs. The gain and phase response of SBS can be calculated from the real and imaginary parts of Eq. (A1), respectively.

Using small signal analysis, the output of the phase modulator fed by an RF signal at an angular frequency ω_{RF} is given by[3]

$$E_{OPM}(t) = E_c\Big[J_0(m)e^{j\omega_c t} - J_1(m)e^{j(\omega_c-\omega_{RF})t} + J_1(m)e^{j(\omega_c+\omega_{RF})t}\Big], \quad (A2)$$

where E_c is the electric field of the optical carrier, m is the modulation index of the phase modulator, and $J_n(\cdot)$ is the Bessel function of nth order.

On considering the separation between the peak SBS gain and loss applied on the USB of the phase modulated link Δx, the combined response can be written as

$$G(\omega) = G_{SBS}\left(\omega - \frac{\Delta x}{2}\right) - G_{SBS}\left(\omega + \frac{\Delta x}{2}\right). \quad (A3)$$

By using a programmable optical filter after the phase modulator, a constant phase shift ϕ_{LSB} is provided on the LSB of the phase-modulated link, and it can be expressed in terms of the transfer function $H_{LSB}(\omega)$ given by Eq. (A4). In addition, after applying SBS gain and loss response on the USB of the phase modulated link, the transfer function is represented by Eq. (A5),

$$H_{LSB}(\omega) = e^{j\phi_{LSB}} \quad \forall\omega < \omega_c, \quad (A4)$$

$$H_{USB}(\omega) = e^{G(\omega)} \quad \forall\omega > \omega_c. \quad (A5)$$

The electric field $E_{opt}(t)$ after the application of the above-mentioned transfer function can be written as

$$E_{opt}(t) = E_c\Big[J_0(m)e^{j\omega_c t} - J_1(m)H_{LSB}(\omega_c - \omega_{RF})e^{j(\omega_c-\omega_{RF})t} + J_1(m)H_{USB}(\omega_c + \omega_{RF})e^{j(\omega_c+\omega_{RF})t}\Big]. \quad (A6)$$

On beating $E_{opt}(t)$ at the photodetector of responsivity R_0, it gives a current corresponding to the intensity of the electric field falling at the input of the photodetector. After filtering higher order terms as well as the DC term results in the following equation:

$$I_{PD} \propto |E_{opt}(t)|^2 = R_0 E_{opt}(t)E^*_{opt}(t) \propto 2R_0 J_0(m)J_1(m)E_c^2 \times \Big\{Re\big(e^{j\omega_{RF}t}H_{USB}(\omega_c + \omega_{RF})\big) - Re\big(e^{j\omega_{RF}t}H_{LSB}(\omega_c - \omega_{RF})\big)\Big\}. \quad (A7)$$

In addition, the gain G_{USB} and phase response ϕ_{USB} imparted on USB can be given by

$$\phi_{USB} = Im(G(\omega_c + \omega_{RF})), \quad (A8)$$

$$G_{USB} = e^{Re(G(\omega_c+\omega_{RF}))}. \quad (A9)$$

Therefore, the photodetector's current after the SBS response is given by

$$I_{PD}(\omega_{RF}) \propto 2R_0 J_0(m)J_1(m)E_c^2\{G_{USB}\cos(\omega_{RF}t + \phi_{USB}) - \cos(\omega_{RF}t + \phi_{LSB})\}. \quad (A10)$$

REFERENCES

[1] J. Capmany and D. Novak, "Microwave photonics combines two worlds," Nat. Photonics **1**(6), 319–330 (2007).

[2] R. Parihar *et al.*, "100 dB microwave photonic filter for communications and RF sensing applications," J. Lightwave Technol. **42**, 7643 (2024).

[3] K. Girish *et al.*, "Low-power, reconfigurable Brillouin RF photonic bandstop filters," IEEE Photonics Technol. Lett. **35**(6), 305–308 (2023).

[4] P. Raj *et al.*, "Energy-efficient bandwidth enhancement of Brillouin microwave photonic bandpass filters," Opt. Express **30**(17), 30739 (2022).

[5] Y. Liu *et al.*, "Integrated microwave photonic filters," Adv. Opt. Photonics **12**(2), 485 (2020).

[6] S. Mahon, "The 5G effect on RF filter technologies," IEEE Trans. Semicond. Manuf. **30**(4), 494–499 (2017).

[7] Y. Yang *et al.*, "X-band miniature filters using lithium niobate acoustic resonators and bandwidth widening technique," IEEE Trans. Microwave Theory Tech. **69**(3), 1602–1610 (2021).

[8] A. Hagelauer *et al.*, "From microwave acoustic filters to millimeter-wave operation and new applications," IEEE J. Microwaves **3**(1), 484–508 (2023).

[9] D. Tiradossi *et al.*, "Planar and low-consumption switchable filter banks with tunable passband and stopband responses," in *2021 IEEE MTT-S International Microwave Filter Workshop (IMFW)* (IEEE, 2021).

[10] A. S. Hussaini *et al.*, "Tunable RF filters: Survey and beyond," in *2011 18th IEEE International Conference on Electronics, Circuits, and Systems* (IEEE, 2011).

[11] R. Parihar *et al.*, "Design of microwave photonic subsystems using Brillouin scattering," J. Lightwave Technol. **39**(4), 977–991 (15 Feb15, 2021).

[12] V. R. Supradeepa *et al.*, "Comb-based radiofrequency photonic filters with rapid tunability and high selectivity," Nat. Photonics **6**, 186–194 (2012) 3.

[13] D. Marpaung *et al.*, "Integrated microwave photonics," Nat. Photonics **13**, 80–90 (2019).

[14] L. Zhuang *et al.*, "Programmable photonic signal processor chip for radiofrequency applications," Optica **2**, 854–859 (2015).

[15] J. S. Fandiño *et al.*, "A monolithic integrated photonic microwave filter," Nat. Photonics **11**, 124–129 (2016).

[16] W. Zhang and R. A. Minasian, "Ultrawide tunable microwave photonic notch filter based on stimulated Brillouin scattering," IEEE Photonics Technol. Lett. **24**(14), 1182–1184 (2012).

[17] D. Marpaung *et al.*, "Integrated microwave photonics," Laser Photonics Rev. 7(4), 506–538 (2013).

[18] W. Bogaerts *et al.*, "Silicon microring resonators," Laser Photonics Rev. **6**(1), 47–73 (2011).

[19] Y. Tao *et al.*, "Hybrid-integrated high-performance microwave photonic filter with switchable response," Photonics Res. **9**(8), 1569 (2021).

[20] O. Daulay *et al.*, "Ultrahigh dynamic range and low noise figure programmable integrated microwave photonic filter," Nat. Commun. **13**(1), 7798 (2022).

[21] T. Carmon *et al.*, "Dynamical thermal behavior and thermal self-stability of microcavities," Opt. Express **12**(20), 4742 (2004).

[22] L. Zhang *et al.*, "Ultralow-loss silicon photonics beyond the singlemode regime," Laser Photonics Rev. **16**(4), 2100292 (2022).
[23] J. Hu *et al.*, "Reconfigurable radiofrequency filters based on versatile soliton microcombs," Nat. Commun. **11**(1), 4377 (2020).
[24] J. V. Sancho *et al.*, "Integrable microwave filter based on a photonic crystal delay line," Nat. Commun. **3**(1), 1075 (2012).
[25] Z. Shi *et al.*, "Tunable single notch microwave photonic filter based on delay lines," Opt. Commun. **448**, 15–18 (2019).
[26] H. Shu *et al.*, "Microcomb-driven silicon photonic systems," Nature **605**(7910), 457–463 (2022).
[27] R. Pant *et al.*, "On-chip stimulated Brillouin scattering," Opt. Express **19**(9), 8285 (2011).
[28] M. Merklein *et al.*, "100 years of Brillouin scattering: Historical and future perspectives," Appl. Phys. Rev. **9**(4), 041306 (2022).
[29] B. J. Eggleton *et al.*, "Brillouin integrated photonics," Nat. Photonics **13**(10), 664–677 (2019).
[30] W. Zou *et al.*, "Complete discrimination of strain and temperature using Brillouin frequency shift and birefringence in a polarization-maintaining fiber," Opt. Express **17**(3), 1248 (2009).
[31] A. Choudhary *et al.*, "Advanced integrated microwave signal processing with giant on-chip Brillouin gain," J. Lightwave Technol. **35**(4), 846–854 (2017).
[32] L. Yi *et al.*, "Rectangular microwave photonic filter based on stimulated Brillouin scattering in fiber," in *2015 14th International Conference on Optical Communications and Networks (ICOCN)* (IEEE, Nanjing, China, 2015), pp. 1–3.
[33] A. Choudhary *et al.*, "Tailoring of the Brillouin gain for on-chip widely tunable and reconfigurable broadband microwave photonic filters," Opt. Lett. **41**, 436–439 (2016).
[34] C. K. Lai *et al.*, "Hybrid chalcogenide-germanosilicate waveguides for high performance stimulated Brillouin scattering applications," Adv. Funct. Mater. **32**, 2105230 (2022).
[35] A. Choudhary *et al.*, "High-resolution, on-chip RF photonic signal processor using Brillouin gain shaping and RF interference," Sci. Rep. **7**(1), 5932 (2017).
[36] J. Shen *et al.*, "High-performance surface acoustic wave devices using $LiNbO_3/SiO_2/SiC$ multilayered substrates," IEEE Trans. Microwave Theory Tech. **69**(8), 3693–3705 (2021).
[37] S. Du *et al.*, "High selectivity and compact tunable bandpass filter using YIG material," J. Appl. Phys. **133**(10), 103901 (2023).
[38] M. Song *et al.*, "Multiband microwave photonic filters with tunability and programmability via optical frequency comb shaping," J. Lightwave Technol. **41**(23), 7215–7222 (1 Dec1, 2023).
[39] W. Zhang and J. Yao, "On-chip silicon photonic integrated frequency-tunable bandpass microwave photonic filter," Opt. Lett. **43**, 3622–3625 (2018).
[40] H. Qiu, X. Zhang *et al.*, "A continuously tunable sub-gigahertz microwave photonic bandpass filter based on an ultra-high-Q silicon microring resonator," J. Lightwave Technol. **36**, 4312–4318 (2018).
[41] M. Tan *et al.*, "Photonic RF and microwave filters based on 49 GHz and 200 GHz Kerr microcombs," Opt. Commun. **465**, 125563 (2020).
[42] S. Gertler *et al.*, "Tunable microwave-photonic filtering with high out-of-band rejection in silicon," APL Photonics **5**, 096103 (2020).
[43] H. Yang *et al.*, "A stopband and passband switchable microwave photonic filter based on integrated dual ring coupled Mach-Zehnder interferometer," IEEE Photonics J. **11**, 5502608 (2019).
[44] Y. Liu *et al.*, "All-optimized integrated RF photonic notch filter," Opt. Lett. **42**, 4631–4634 (2017).
[45] B. J. Eggleton *et al.*, "Inducing and harnessing stimulated Brillouin scattering in photonic integrated circuits," Adv. Opt. Photonics **5**(4), 536 (2013).
[46] C. G. Poulton *et al.*, "Acoustic confinement and stimulated Brillouin scattering in integrated optical waveguides," J. Opt. Soc. Am. B **30**(10), 2657 (2013).
[47] M. Garrett *et al.*, "Integrated microwave photonic notch filter using a heterogeneously integrated Brillouin and active-silicon photonic circuit," Nat. Commun. **14**(1), 7544 (2023).